Volumetric velocity measurements in restricted geometries using spiral sampling: a phantom study.

Nilsson, Anders; Revstedt, Johan; Heiberg, Einar; Ståhlberg, Freddy; Markenroth Bloch, Karin

Published in:
Magma

DOI:
10.1007/s10334-014-0449-0

2015

Citation for published version (APA):
Nilsson, A., Revstedt, J., Heiberg, E., Ståhlberg, F., & Markenroth Bloch, K. (2015). Volumetric velocity measurements in restricted geometries using spiral sampling: a phantom study. *Magma*, *28*(2), 103-118. https://doi.org/10.1007/s10334-014-0449-0

Total number of authors:
5

Volumetric velocity measurements in restricted geometries using spiral sampling: a phantom study

Nilsson Anders, Revstedt Johan, Heiberg Einar, Ståhlberg Freddy,

Markenroth Bloch Karin

Affiliations:

AN: Department of Medical Radiation Physics, Lund University

JR: Department of Energy Sciences, Lund University

EH: Department of Clinical Physiology, Lund University, Lund University Hospital, Lund, Sweden.

Centre for Mathematical Sciences, Lund University, Sweden

FS: Department of Medical Radiation Physics, Lund University

Department of Radiology, Lund University

KMB: Philips Healthcare, Lund, Sweden

Corresponding author: anders.nilsson@med.lu.se

Telephone: +46 46 173132

Fax: +46 46 178540

Word count of abstract and text: 7129

No. of Figures/tables: 9/4

No. of References: 56

Abstract

Object:

To evaluate the accuracy of maximum velocity measurements using volumetric phase contrast imaging with spiral readouts in a stenotic flow phantom.

Materials and Methods:

In a phantom model, maximum velocity, flow, pressure gradient and streamline visualizations were evaluated using volumetric phase contrast MRI with velocity encoding in one (extending on current clinical practice) and three directions (for characterization of the flow field) using spiral readouts. Results of maximum velocity and pressure drop were compared to CFD simulations (Computational Fluid Dynamics), as well as corresponding low-TE Cartesian data. Flow was compared to 2D throughplane PC upstream from the restriction.

Results:

Results obtained with 3D throughplane PC as well as 4D PC at shortest TE using spiral readout showed excellent agreements with the maximum velocity values obtained with CFD (<1% for both methods), while larger deviations were seen using Cartesian readouts (-2% and 13%, respectively). Peak pressure drop calculated from 3D throughplane PC and 4D PC spiral sequences was 14% and 13% overestimated compared to CFD.

Conclusion:

Identification of the maximum velocity location as well as accurate velocity quantification can be obtained in stenotic regions using short-TE spiral volumetric PC imaging.

Introduction

Measurement of blood flow and blood velocity in stenotic vessels can be used for pressure estimation and subsequent classification of the severity of the occlusion, which can guide the treatment decision [1,2]. A key parameter when estimating pressure gradients over a stenosis is the maximum velocity of the blood during systole, from which the peak pressure gradient can be derived using the simplified or modified Bernoulli equation [3,4]. Accurate determination of the maximum velocity in a stenotic jet is thus of clinical importance for correct assessment of the severity of the occlusion.

Currently, the most common method for estimating orifice area and maximum velocities is Doppler echocardiography (DE) [5]. Although well-established, DE as a technique has a number of limitations, such as the need for correct angulation between the Doppler beam and the flow jet and dependence on the geometry of the restriction [4,6].

An alternative non-invasive method for blood velocity measurements is phase contrast MRI (PC-MRI). Velocity measurements with PC-MRI have been reported to underestimate maximum velocities in certain stenotic vessel geometries, while presenting a good correlation in other cases [7]. Uncertainties may, for example, be related to limited spatial and temporal resolution, inherent SNR limitations, as well as intra-voxel dephasing and unsteady flow where higher-order motion is present [8]. In particular, the high velocities and complex flow patterns found in restricted geometries require short echo times in order to reduce intra-voxel phase dispersion and signal drop in magnitude images. Hence, early studies showed the usefulness of short-TE 2D throughplane PC for stenotic flow measurements [9,10]. Recent investigations using 2D throughplane PC for pressure estimation have also proven successful in clinical application, and confirmed the need for short echo times [11-13].The necessity to reduce echo times suggest the combination of phase-contrast with a non-Cartesian readout scheme, such as radial or spiral readouts, as these sequences begin their k-space traversal in the centre of k-space, thus reducing the time between excitation and sampling. Ultra-short echo time sequences (UTE sequences) in combination with radial readouts have recently been shown to improve velocity and flow measurements in restrictions in vitro as well as in vivo using sub-millisecond echo times [14]. Depiction of flow jets with short spiral readouts has also been successfully performed [15]. A further advantage of non-Cartesian sequences is that in-plane spatial encoding occurs at a single point in time, while timing for readout and phase encoding differ in Cartesian sequences, which can introduce errors and artifacts [16]. A drawback of using spiral trajectories is that the temporal proximity of encoding gradients to the readout of the centre of k-space is expected to increase background phase offsets. However, background phase offsets arising from eddy-currents could be corrected for using several strategies [17-19].

One evident difficulty with 2D throughplane PC techniques in the context of restrictions is to measure at the true position of the maximum velocity. Hence, in several 2D throughplane PC studies of maximum velocity and flow determinations in stenotic vessels, a multi-slice procedure was used [11,20]. With the advent of three-dimensional, three-directional velocity encoding sequences (here denoted 4D PC) [21-23], the possibility has emerged to quantify velocity and flow in multiple dimensions, and in addition to visualize blood flow by streamlines and pathlines. These powerful possibilities offered by 4D PC have found a number of applications, and 4D PC has started to go beyond a visualization tool into a quantitative technique for extraction of velocity, flow and hemodynamically derived parameters such as wall shear stress [24] and kinetic energy [25]. 4D PC sequences also holds potential to a variety of clinical applications, such as detection of abnormal blood flow [26] and aortic valve coarctation [27]. A major obstacle to wide-spread clinical use of 4D PC is the long acquisitions times. However, volumetric non-cartesian sequences in combination with PC (such as PC-VIPR) have been shown able to greatly reduce acquisition times compared to traditional Cartesian readout schemes, while maintaining accuracy in flow quantification [28,29], and 4D PC have also been successfully combined with spiral readouts for *in-vivo* measurements [30,31].

Recently, multi-dimensional investigations of velocity and flow in restrictions associated with high-velocity jet streams have been reported in clinical data [32-34]. Volumetric 4D PC sequences also offer the possibility to track the position of a restriction over the cardiac cycle. The combination of volumetric PC sequences and spiral readout therefore seems suitable for restricted geometries.

After a restriction, a jet is formed which opens the possibility to use a volumetric method, but with velocity encoding only along the direction of the jet (3D throughplane PC). Neglecting the other velocity components could potentially reduce imaging times by 50% without losing the crucial information, which is the maximum velocity in the stenotic jet. This approach would be an extension of the multi-acquisition 2D throughplane PC reported [11,20], with the benefit of control over relative slice positioning and simultaneous acquisitions. However, studies characterising the behaviour of 3D throughplane PC and 4D PC sequences in controlled, restricted geometries are sparse [35,36], warranting a thorough phantom study of properties and performances of different types of sequences.

Therefore, the purpose of this work was to utilize the large coverage of volumetric PC sequences in order to find the position of the jet and measure the maximum velocity in a controlled phantom geometry using spiral readout schemes , and to compare the results with CFD simulations as well as theoretical values. For additional comparison, 3D throughplane PC as well as 4D PC with Cartesian readout using the shortest possible TE were also included.

Materials and Methods

All measurements were performed on a 3T Achieva MR scanner (Philips Healthcare, Best, the Netherlands) with a six-channel cardiac coil. The maximum gradient strength was 31 mT/m for PC sequences, with a maximum gradient slew rate of 180 mT/m/s.

The phantom consisted of a water-filled plastic cylinder (diameter 150 mm, length 300 mm) encompassing two parallel, straight plastic tubes (inner diameter 21 mm, length 400 mm) positioned along the axis of the cylinder, with equal but oppositely directed water flow (Fig 1). One of the tubes contained a 6 mm thick concentric restriction with an orifice diameter of 9 mm, giving an area reduction of 82 % compared to the open tube. The restriction was positioned in the central part of the phantom, resulting in approximately 200 mm of undisturbed flow before as well as after the restriction.

The tubes in the phantom were positioned parallel to the feet-head direction in the MR scanner, with the restriction placed in the magnet isocentre.

Gadolinium-doped water was pumped through the phantom at constant flow rate by a home-built pump system, consisting of a water pump (Biltema, Sweden) submerged in a water tank and connected to one of the phantom tubes, while the other tube transported water from the phantom back to the water tank in a recirculating flow system.

All PC sequences were based on a spoiled gradient-echo sequence with TE-optimized velocity encoding [37]. The PC sequences used volume excitation with a flip angle of 10°. The slice selection direction (z) was aligned with the direction of flow (feet-head direction) for all sequences. Two different sampling schemes were applied: 1) a conventional Cartesian readout, and 2) a spiral readout with the spirals aligned with the k_x-k_y-planes (a “stack of spirals” sampling scheme). The read-out time for each spiral was kept short (2.5 ms), in order to avoid flow artifacts [15]. The number of spiral interleaves in each k_x-k_y-plane was set to 80. For both 3D throughplane PC- and 4D PC sequences, four phase encoding steps were collected in each acquired timeframe (turbo-factor equal to 4).

For both Cartesian and spiral sampling, two different velocity encoding strategies were investigated: (i) 3D throughplane PC, where velocity encoding was performed only in the main direction of flow, perpendicular to the imaging planes, and (ii) 4D PC with velocity encoding in three orthogonal directions, allowing for reconstruction of the complete velocity field and subsequent visualizations.

The 3D throughplane PC and 4D PC sequences with spiral readouts were studied over a range of echo times (see Table 1a and Figure 2). 3D throughplane PC and 4D PC sequences with Cartesian readout were only performed with the shortest possible echo time, and used for comparison with the spiral data. When TE was increased, the durations of the spatial- and velocity encoding gradients were extended in order to fill up the increased time (Figure 2). The acceleration sensitivity, expressed as the acceleration inducing a phase shift equal to π radians, was calculated for each 4D spiral sequence as the remaining difference in second order moment after each velocity encoding segment was integrated between excitation and TE with respect to second order gradient moment (Table 1b).

The 3D throughplane sequences were examined both as cardiac triggered and untriggered, using a simulated VCG signal for synchronization of the triggered datasets, while the 4D PC sequences were examined triggered. The time frames of the triggered datasets were subsequently used for statistical evaluation.

Due to the time consuming nature of the volumetric velocity measurements, these were divided into three scan occasions, in which identical phantom setup was used. In each of three scan sessions, one or several conventional, high-resolution 2D throughplane PC sequences with through-plane velocity encoding were performed to serve as reference flow measurements for the 3D throughplane PC and 4D PC data acquired in that session. The non-segmented 2D throughplane PC sequence used as a flow reference has previously been evaluated on the scanner system [38]. To acquire the 2D throughplane PC reference flow data, the single slice was positioned approximately 5 cm (~2.5 pipe diameters) before the restriction, a position where the flow profile was considered to be unaffected by the restriction. As the reference slice also contained data from the opposite tube that did not have any restriction, the validity of this assumption was inherently checked. The reference flow rate was calculated as the mean of the absolute flow values obtained in the two open tubes. The reference flow rates differed a few percent between the scan sessions, and in the results presented, care has been taken to use the correct reference value for each sequence. In Table 1a, an overview of sequences and sequence parameters are given.

Data processing and evaluation

Background phase correction was performed offline after acquisition for all volumetric sequences. Using Matlab R2011a (The Mathworks, Natick, MA), the phase of the static areas in the images was fitted to a 3D linear function, and this fit was subtracted from the data, as previously described [17]. Selection criteria for static tissue were the following: voxels with a magnitude intensity of at least 15 % of the maximum intensity and with a velocity magnitude below a certain limit (15-30 cm/s) were considered stationary and used for fitting. The 2D throughplane PC sequences used for flow reference measurements were acquired using the phase correction routines provided by the manufacturer, and were not further corrected for background phase offsets.

ROI definitions, velocity and flow measurements were performed in GTFlow 1.6.8 (Gyrotools Inc., Zurich, Switzerland). Slices positioned within the restriction were identified by the visually observed reduction of magnitude signal from the plastic disc constituting the restriction, and the slice having the lowest magnitude signal was considered to be in the most central position of the restriction. The ROI definition in the restriction was performed by averaging line-profiles of measured through-plane velocities in the Anterior-Posterior (AP) and Right-Left (RL) direction. The averaged Full-Width-at-Half-Maximum (FWHM) of the line profiles was chosen as the diameter of the circular ROI prescribed for evaluation [9]. For measurements upstream and downstream of the restriction, a circular ROI with area equal to the known nominal inner dimension of the tube was used. In both cases, voxels whose geometric centres lay inside the drawn ROI contour were included in the ROI analysis.

The numbers of voxels with erroneous velocity values inside the ROI definitions were compared for the sequences used. Comparisons were performed including all acquired slices and timeframes. Voxels with erroneous values were defined as voxels having a velocity exceeding 0.5·VENC, i.e. 250 cm/s, directed opposite to the jet flow direction (-Z direction).

For the 3D throughplane PC datasets, maximum velocity was defined as the maximum velocity found inside the ROI definitions in the forward direction along the axis of the phantom cylinder. For the 4D PC datasets, maximum velocity was calculated as the maximum velocity magnitude inside the ROI definitions. Net flow was calculated in each slice as the product of average forward velocity within the ROI and the ROI area.

Maximum pressure gradient across the restriction was calculated using the simplified Bernoulli formula;

$$\Delta P_{max} = C(\rho) \cdot v_{max}^2 \qquad \text{[mmHg]} \qquad (1)$$

in which v_{max} is the maximum velocity in the direction of the jet found in the ROI of the central slice. The density of water gives $C(\rho)$ = 3.75, while $C(\rho)$ for blood is 4.

From the data acquired with the 4D PC sequences, streamline visualizations were created in GTFlow by seeding streamline seeds in the centre of the restriction and tracking forwards as well as backwards in the velocity field.

Vena contracta velocity determination

Due to the geometry of the restriction, it can be assumed that there exists a region containing the highest velocity caused by the restriction, called *vena contracta,* which coincides with the position of the lowest pressure along the restriction. The concept of *vena contracta* is further explained by Massey [39]. If the shape of the restriction is circular and sharp-edged, which is fulfilled for the current setup, the presumed maximum velocity $v_{vc,max}$ in *vena contracta* can be estimated from the reference flow (Q), the orifice area (*A*), and a correction factor C_d (coefficient of discharge), adopted for thick-plate geometries [40,41]:

$$v_{vc,max} = \frac{Q}{A \cdot C_d} \qquad (2)$$

The correction factor C_d was extracted from ref [41], and for this particular geometry was found to be C_d = 0.59.

CFD simulations

The measured reference flow from the 2D throughplane PC measurements were used as input to CFD simulations. The CFD simulations were performed using ANSYS Fluent 14 (Ansys Inc., Canonsburg PA). The governing equations were discretized using a second order finite volume method, and the pressure-velocity coupling was done using the SIMPLE algorithm [42]. The computational geometry is a two-dimensional axisymmetric representation of the tube, 40 tube diameters long. The stenosis was placed midway between inlet and outlet.

A steady axial velocity with no variation in the radial direction was set at the inlet (v_{inlet}=0.473 m/s and v_{inlet}=0.462 m/s), corresponding to measured reference flows of 165 ml/s and 161 ml/s as measured in the same scan session as the triggered 3D throughplane PC sequences and the triggered 4D PC sequences, respectively. The turbulence intensity at the inlet was set to 10% and the turbulent length scale to half of the tube radius. A fully developed turbulent velocity profile was achieved at about 3 pipe diameters upstream of the stenosis centre. At the outlet, Neumann conditions were used for all variables and no-slip conditions were set on the tube wall. Three turbulence models were considered; the RNG k-ε model [43], the k-ω SST model [44] and a differential Reynolds stress model (RSM) using a quadratic pressure-strain model [45]. The near wall turbulence in the k-ε and k-ω models was handled using the 'enhanced near wall treatment' option and for the RSM the 'scalable wall functions' option was used.

A structured mesh consisting of 119392 nodes was used, and the mesh was refined towards the walls of the tube and restriction. In order to investigate the mesh sensitivity of the solution, simulations were performed on meshes with 22316 (Mesh 1), 119392 (Mesh 2) and 447305 (Mesh 3) nodes. The difference in maximum centre line velocity was about 4% between Mesh 1 and Mesh 3 and less than 2% between Mesh 2 and Mesh 3.

Considering the results from simulations with the different turbulence models (using Mesh 2) one finds that the maximum velocity is about 7 % lower for the RNG k-e model than for the RSM and the k-ω SST model. Furthermore, the k-ω SST model predicts a significantly longer jet than the RNG k-e and the RSM. Both the RNG k-ε model and the k-ω SST model make use of the turbulent viscosity hypothesis, in which the Reynolds stress tensor is calculated from the mean rate of strain [46]. This approach is known to give less accurate results in several flow situations including those containing rapid changes in mean rate of strain, such as flows with a constriction. An in depth discussion on these matters can be found in [47]. The RSM, on the other hand, does not rely on this hypothesis and instead contains a set of partial differential equations for the Reynolds stress tensor. Hence, an RSM with a non-linear pressure-rate of strain formulation would be the best choice, of the three models investigated, in order to obtain results with good accuracy for the flow situation considered here. Hence, in the following simulation results from the RSM are presented.

The highest velocity in the forward direction along the axis of the phantom cylinder found inside the orifice was considered the CFD-derived maximum velocity ($v_{CFD,max}$).

The maximum pressure gradients calculated from Eq. [1] above were compared to the corresponding maximum pressure gradient along the central axis derived from the CFD simulations, here calculated as the difference between the pressure 30 mm upstream from the restriction and the minimum pressure found across the restriction.

Statistical evaluation

Flow and maximum velocity measurements from the triggered sequences were averaged over time frames, and the corresponding standard error of the mean were calculated.

Results

Image characteristics

For all datasets, the highest magnitude signal intensities were found immediately prior to the restriction. Distal to the restriction, magnitude signal intensities in the spiral datasets were seen to decrease with increasing TE, in 3D throughplane PC as well as 4D datasets. As an example, the untriggered 3D throughplane PC sequences are shown in Fig. 3. The signal decrease was most prominent along the borders of the jet. Magnitude signal intensity was maintained in the jet core for all investigated TE for the spiral sequences, indicating ordered motion in the centre of the jet. Corresponding images of the 4D PC datasets presented similar changes in magnitude and velocity images when TE was increased.

Voxels with obviously erroneous velocity values occurred only in spiral datasets with TE ≥ 3 ms, and coincided with the low-signal regions, i.e. along the borders of the jet close to the restriction. The number of erroneous voxels increased when TE was extended to 4 ms. At echo times shorter than 3 ms, only 3D throughplane PC and 4D PC sequences with Cartesian readout presented voxels with erroneous velocities, positioned at the edges of the restriction.

Flow

The reference flow as measured by 2D throughplane PC, averaged over all measurements and both pipes at each of the three scan sessions, was found to be 171 ml/s, 165 ml/s, and 161 ml/s, respectively. For all three occasions, the flow was equal in both tubes within 1 ml/s and in the range of corresponding manual flow measurements performed with timer and beaker.

Fig. 4 shows the measured flow as a function of position along the Z axis, measured with triggered 3D throughplane PC (Fig. 4a) as well as triggered 4D PC (Fig 4b) for a range of echo times. For 3D throughplane PC sequences, flow deviated -0.6% (Cartesian) and 12% (spiral) at shortest echo times, while the deviation for the 4D datasets was 27% for Cartesian readout and and 0.8% for spiral readout (Table 2a). Increasing TE resulted in higher deviations compared to reference flow (Table 2b).

In general, measured flow downstream from the orifice presented a higher deviation from the reference flow when TE was increased, as seen in Fig. 4. Spiral sequences show what seemed to be a systematic underestimation of flow of about 10-15% even for the lowest TE, which increased with downstream distance from the restriction. For longer echo times, erroneous velocity values from the regions with low magnitude intensities contributed to the drop in measured flow immediately downstream from the restriction. At shortest possible echo times and at a short distance after the restriction, both Cartesian and spiral sequences presented flow values in reasonable agreement with the reference value. Measured flow just before the restriction was underestimated for both Cartesian and spiral sequences.

Maximum velocity

Measured maximum velocities (v_{max}) in the center of the restriction are summarized in Table 2b, together with maximum peak pressure gradients calculated using Eq. 1.

Fig. 5 shows the maximum velocity as a function of distance along the Z axis from the restriction for triggered 3D throughplane PC (Fig. 5a) and 4D PC (Fig. 5b) measurements. Fig. 5 also displays the maximum velocity derived from CFD simulations ($v_{CFD,max}$) and the theoretically derived *vena contracta* velocity ($v_{VC,max}$) obtained by Eq. [2]. Due to the thick plate used in the experiments, which deviates from the thin-plate assumptions often used in the literature, the theoretically derived position of the *vena contracta* is uncertain. Therefore, an approximate position for $v_{VC,max}$ was chosen in Fig. 5, and set to ±3 mm around the orifice centre, i.e inside the orifice. The $v_{VC,max}$ was calculated to 4.25 m/s (flow 161.4 ml/s) and 4.35 m/s (flow 165.5 ml/s), respectively.

For the lowest TE, v_{max} measured with the 3D throughplane PC sequences with Cartesian as well as spiral readouts was positioned in the centre of the restriction, and coincided along the Z axis with both the position of $v_{CFD,max}$ and the presumed position of *vena contracta* (Fig 5a). For the 4D PC datasets with spiral readout and TE=1.44 ms and 2 ms, the maximum velocity was found in the central slice covering the restriction, while for the other 4D PC sequences v_{max} was found distal to the restriction (Fig 5b).

The measured maximum velocity measured with 3D throughplane PC showed small deviations from $v_{CFD,max}$ (-2.3% for Cartesian readout, -0.1% for spiral readout with shortest TE). Corresponding maximum velocity measured with 4D PC spiral sequence presented excellent agreement (-0.5% deviation), while the deviation was higher for the 4D PC dataset with Cartesian readout (13%). Again, v_{max} was seen to increase with increasing echo time (Table 2b).

Fig. 6 shows the results from the CFD simulation of the velocity field. The highest velocity magnitude derived from CFD simulations ($v_{CFD,max}$) was located inside the restriction and was found to be 4.06 m/s (flow 161.4 ml/s) and 4.15 m/s (165.5 ml/s), respectively. This maximum velocity was not situated on the central axis through the restriction, but rather close to the walls of the orifice (1.3 and 1.2 mm from the orifice wall, 3.1 mm and 0.7 mm before the centre of the orifice for flow 161.4 ml/s and 165.4 ml/s, respectively) where the incoming flow converged (before the line profile displayed in Fig. 6).

CFD simulations revealed a position with smallest effective area of the jet in the range 1.3 mm upstream to 0.7 mm downstream of the orifice centre for both simulated flow volumes. By definition, *vena contracta* should be located in that range.

In a plane perpendicular to the central axis across the centre of the restriction (displayed as the line profile in Fig. 6), CFD simulations presented the highest velocity magnitude (4.05 m/s for flow 161.4 ml/s, and 414 m/s for flow 165.4 ml/s) close to the walls of the orifice, and a velocity magnitude of 3.71 m/s (flow 161.4 ml/s) and 3.79 m/s (flow 165.4 ml/s) respectively in the centre of the orifice (solid line). The plots illustrate that the measured velocity in the centre of the orifice is well replicated by both 3D throughplane PC sequences (Fig 6a) and 4D PC sequences (Fig 6b), although the relatively coarse spatial resolution of the MR measurements cannot capture the concave top of the CFD profile.

In Fig. 7, the average velocities on the central axis as a function of distance from the restriction are shown for both triggered 3D throughplane PC measurements (Fig 7a) and triggered 4D PC measurements (Fig 7b), along with CFD-derived velocity. All 3D throughplane PC datasets underestimated the average centreline velocity, while better resemblance was observed for 4D PC datasets with short TE (Fig 7b). The CFD-derived velocity in the direction of the jet on the central axis was seen to form a plateau downstream of the orifice (approximately 5 – 30 mm after the orifice), at which the central axis velocity was only slowly decreasing (Fig. 7). At ~45 mm downstream of the orifice, the rate of decrease in velocity along the central axis became higher. For all datasets, a corresponding plateau of slow velocity decrease immediately downstream of the restriction was observed, while the region of rapid velocity reduction occurred more upstream than predicted by the CFD-simulations. However, it is evident from Fig. 7 that the MR-measurements of average velocity agree well with the CFD simulations up to 5-10 slices after the restriction.

Pressure gradients

The minimum pressure derived from the CFD simulations was found 2 mm downstream from the orifice centre, i.e. inside the restriction, for both simulated flow volumes. The CFD-derived maximum pressure gradient, calculated from the pressure before the restriction and the minimal pressure, was found to be 54 mmHg (at flow rate 161.4 ml/s) and 57 mmHg (at flow rate 165.4 ml/s).

Compared to these values, the maximum pressure gradients from MR data and derived from Eq. 1 was overestimated for all triggered sequences, using the shortest possible TE as well with higher echo times (Table 2a, Table 2b). The 3D throughplane sequence with Cartesian readout presented lowest deviation (8.8%), while corresponding spiral sequence deviated 14%. The pressure gradient derived from the 4D PC sequences deviated 48% for Cartesian readout and 13% for spiral readout, respectively. For longer echo times, deviation of measured peak pressure gradients increased, reaching an overestimation of 50% for the 4D PC spiral sequence at TE=4 ms (Table 2b).

3D- and 4D visualization

Fig. 8 presents contour plots of the jet from the 3D throughplane PC sequences, while Fig. 9 shows streamline visualizations performed using the 4D PC data sets. At shortest TE, the Cartesian 3D throughplane PC dataset presented a wider jet than the spiral counterpart. When TE was increased to 4 ms, the spiral dataset presented a more skewed contour with higher velocities in the central part of the jet, as observed in Fig 5.

The streamlines created from the 4D PC Cartesian dataset with shortest possible TE presented a larger amount of streamlines lost from the jet than for any spiral 4D PC dataset (Fig 9a). Corresponding streamlines from data of the 4D PC datasets with spiral readouts had symmetrical and similar shapes for all echo times (Fig 9b-e), but also presented a small drift upwards in Y direction. As observed previously, the velocity in the centre of the jet was elevated and shifted downstream with increasing TE.

Discussion

In this work, we have shown that low-TE volumetric PC sequences with spiral readouts are able to accurately measure maximum velocities as compared to CFD-derived maximum velocity. We also confirmed the benefit of using low TE to reduce the deviation in measured flow, maximum velocities and pressure gradients for volumetric measurements.

Stenotic flow fields are problematic to depict and measure with PC-MRI, due to the inherent high velocities and complex flow patterns causing well-known dephasing effects. Although the signal drop related to high-speed jets may ease their identification *in-vivo*, quantitative velocity images can be expected to be affected by varying velocities present in turbulent regions, due to the fact that the subtracted image segments are measured sequentially and therefore experience different velocity fields when complex and unsteady flow is present [48]. Nevertheless, using low echo times has proven to be a way forward in 2D throughplane PC of stenotic flow fields, but with the drawback of using only single- or at best multiple slices. While 2D throughplane PC is still the current clinical practice to measure maximum velocities, the transition to volumetric PC sequences seems desirable, as these sequences offer better volume coverage and thus enables a better localization of the maximum velocity. Similar to 2D throughplane PC, 3D throughplane PC measures only the throughplane velocity, with the requirement of additional acquisition time. It provides better control of relative slice positioning and thinner slices than the method of repeated 2D throughplane PC examinations, in a shorter scan time than 4D PC.

However, the measurement of only the throughplane velocity requires the velocity encoding direction to be aligned with the presumed direction of the highest velocity. The 3D throughplane PC sequence may be clinically useful e.g. in carotid artery disease and aortic coarctations, where the slices can be positioned perpendicular to the jet in the region where maximum velocity is expected. 4D PC measures the full velocity vector in the volume, at the cost of longer acquisition times compared to both 2D- and 3D throughplane PC. Additionally, each timepoint in 4D PC requires the sequential collection of four segments, each with different velocity encoding along the spatial coordinates, in order to reconstruct the velocity field. This collection reduces the temporal resolution by a factor of 4.

Magnitude information

Marshall [36] compared CFD simulations with a 4D PC sequence in a human bifurcation phantom model, and reported an increase in signal intensity at regions with high flow velocities. Our phantom results confirm this observation, as the largest signal intensity was found immediately before the restriction. This effect, as mentioned by Marshall, arises from unsaturated spins entering the volume.

We observed a more extensive signal drop in the Cartesian sequences compared to the spiral sequences at comparable echo times, confirming that spiral readouts show less sensitivity to complex flow and dephasing effects. For both readout methods, the signal drop was most pronounced along the borders and downstream of the jet where voxels contain a broad range of motion.

Flow

An advantage of volumetric sequences is the possibility to measure the flow upstream or downstream of the restriction, while the maximum velocity can be simultaneously measured at the correct position. In this work, it was seen that accurate flow quantification is difficult to achieve in the central part of the orifice. Our results confirmed that a low echo time is of importance when quantifying flow in restricted geometries also in volumetric sequences. A major source of error is the high proportion of voxels in the restriction which are affected by the orifice walls, giving substantial partial volume effects. To overcome these partial-volume effects, we used a method of adjusting the size of the ROI with the FWHM of the velocity profile over the orifice. While this method eliminated most of the edge voxels with arbitrary phase values, the method was sensitive to the velocity profile and therefore resulted in larger ROI areas for increasing echo times. Furthermore, rapid spatial changes in velocity properties and saturation effects upon entering the restriction may also contribute to low accuracy. In the light of the ROI sizes smaller than the physical size of the restriction, it is not unexpected that measured flow is underestimated when measured in the centre of the restriction.

Flow measurements downstream of the stenosis were also seen to increasingly deviate when TE was increased. The main contribution to this deviation was voxels in regions with low magnitude intensities having erroneous velocity values. Distal to the restriction, the borders of the flow jet exhibited to a reduction of signal intensity, which occurs due to the intravoxel dephasing, and renders a more uncertain phase values for those voxels.

Maximum velocity and pressure

Comparison of single-directional velocity encoded (3D throughplane PC) and three-directional velocity encoded (4D PC) volumetric sequences showed that both methods were capable of measuring maximum velocities within the range of -0.1 - 13 % from the CFD-derived maximum velocity at lowest possible echo time. For measurements of maximum velocities, it should therefore be noted that 3D throughplane PC presents a less time-consuming alternative than 4D PC, while giving a larger coverage and better resolution along the jet than 2D throughplane PC. However, the limited resolution in the slice direction does not allow for a more precise determination of the location of the maximum velocity inside the restriction in our phantom setup. A higher resolution in the slice direction might prove useful to avoid averaging effects over a large voxel that might obscure the true maximum velocity, but comes at the cost of lower signal-to-noise ratios which may render the measurements of maximum velocity more uncertain.

The observed increase in maximum velocity when TE was prolonged is likely to arise because of the change in higher order moments. According to Table 1b, second order moments are affected when TE is increased, thus making phase contributions from acceleration larger in sequences with long TE as previously observed [49-51].

In various studies with 2D throughplane PC, a location downstream of the restriction has been used for maximum velocity measurements [1,52,14]. O`Brien *et al* [13] used single-slice PC to measure maximum velocities in patients with aortic stenosis, and while finding the majority of the highest velocities in the centre of the stenosis, only found small variations when measured downstream. Although our results from MR with the lowest echo time as well as from CFD indicate that the highest velocity is found inside the stenosis, our CFD simulations also confirm the existence of a region downstream (approximately 5 – 30 mm) in which the velocity at the central axis only decreases slowly.

After this region, the velocity on the central axis falls more rapidly, and measurements here would not be representative of the maximum velocity in the restriction. All sequences presented this drop in central axis velocity closer to the restriction than predicted by CFD simulations. This observation has also been reported elsewhere [35], and this decrease in velocity more close to the restriction may be due to the turbulent region downstream.

According to the fluid mechanics around thin plates, a region with the smallest effective flow area and thus highest average velocity inside the jet (*vena contracta*) is formed immediately downstream from the orifice centre [39]. Considering a thick plate orifice, such as the one used in this work, a *vena contracta* could be formed inside the orifice [40]. Our CFD simulations revealed that a *vena contracta* which contained the narrowest effective diameter of the jet is located inside the orifice for both flow volumes simulated. The exact position of the *vena contracta* was not possible to determine from the simulation data since the variation of effective flow area inside the orifice is very small. However, we found that it is located somewhere in the range from 1.3 mm upstream to 0.7 mm downstream of the orifice centre. Although not a necessity, but this position did not present the maximum velocity, which instead was located near the wall of the orifice at 3.1 and 0.7 mm upstream from the orifice centre, respectively, for the two flow volumes simulated. Neither does it represent the location of minimum centre line pressure (and hence maximum centre line speed) which is found 2 mm downstream of the orifice centre, thus slightly after the CFD-derived position of *vena contracta*.

The flow situation caused by the sharp edges of the plate in combination with the thickness of the orifice is likely the reason for the position of the maximum velocity was not found on the central axis of the restriction, and instead close to the edges of the orifice, and that the position of minimum centre line pressure was not found at the *vena contracta* location. At lowest possible echo time, both Cartesian and spiral sequences presented the maximum velocity in the central slice (covering the orifice), in agreement with the position of both the CFD-derived maximum velocity, CFD-derived position of the minimal pressure, and the CFD-derived position of *vena contracta* when the slice thickness of the MR datasets (3 mm) is taken into account. However, the limited spatial resolution and slice thickness of the MR datasets prevented possible differentiation between the CFD-derived positions of the maximum velocity and *vena contracta*, respectively. The thick voxels are also expected to affect the streamline visualisations, making the spread in traces less due to the averaging effect.

The maximum pressure gradients, derived from the measured maximum velocities, were seen to be overestimated compared to the corresponding maximum pressure gradients derived from the CFD measurements. The simplified Bernoulli equation, Eq. 1, used in this work is often used in clinical routine, but contains a number of assumptions. One simplifying assumption is that the square of the velocity before the restriction is considerably lower than the square of the maximum velocity in the restriction. In our experiments, the average velocity before the restriction was approximately 0.48 m/s. Neglecting the velocity before the restriction induced a slight overestimation of the peak pressure gradients on the order of 1% in our experimental setting.

Another simplification of Eq. 1 is that kinetic losses are neglected. In our stenotic phantom, the restriction contained sharp edges, which contributes to increased turbulence and energy dissipation downstream of the orifice [53]. This was confirmed by the observation that the pressure drop from the CFD simulations corresponded with the pressure drop calculated by the simplified Bernoulli equation in regions before and in the orifice, while it started to deviate further downstream from the orifice where most of the energy dissipation occurs. Furthermore, the CFD-derived pressure drop was found to be heavily geometry-dependent. Performing corresponding CFD simulations after the edges of the orifice had been rounded (rounding radius 0.6 mm) revealed a pressure drop of approximately 26 mmHg, roughly the half of the pressure drop for the original geometry. The distortion in the jet shape found in Cartesian sequences as seen in Fig. 8 can be related to the timing of position and velocity encoding in the sequence [16]. In the Cartesian sequences the positional encoding in the directions perpendicular to the jet occurs at different time points, whereas in the spiral sequence no such time difference exists. Likewise, the difference in time between the traversal of the k-space centre and the effective velocity encoding time [54] is considerably larger in the Cartesian sequences compared to the spiral sequences, which could contribute to the distortion of the jet visualization. The streamline visualizations performed with 4D Cartesian PC (Fig 9a) presented a higher dispersion with more streamlines exiting the jet as well as the tube compared to the 4D sequences with spiral readout (Fig 9b-e). Phase background offsets varied between sequence type and echo time used. As expected, lower background phase offsets were observed in the Cartesian sequences, whereas the spiral sequences presented higher background phase offsets for lower TE. One reason for the observed difference in background phase between the two readout schemes is likely the shorter time delay between the velocity encoding gradient lobes and the k-space central traversal in the spiral sequences. Recent studies of background velocity offsets have shown that eddy-current induced background phase offsets are temporally oscillating [18], which suggests that sequence optimizations with respect to gradient amplitudes, timing, and slew rates should be performed for reducing background phase offsets.

Limitations of this study

Measurements of maximum stenotic velocities *in-vivo* require sufficient temporal resolution, as the maximum velocity will only occur during the systolic part of the cardiac cycle. Because of the use of constant flow rates in this study, the sequences were not optimized for maximal temporal resolution. To achieve sufficient temporal resolution, the FOV in the direction of the jet could be reduced to half (30 mm) while still maintaining a sufficient coverage of the region where the maximum velocity would occur.

In connection to this work, the two sequence types were validated and optimized in a flow phantom setup with undisturbed flow. Results revealed that the spiral sequence suffered from a systematic underestimation of measured flow by 10 - 15 %, as also indicated in Fig. 6b, 6d. Further investigation is needed to fully understand the source of this deviation.

The results are compared to CFD simulations, based on reference flow values. Uncertainties in the reference flow would propagate into the derived maximum velocities and pressure drops. Therefore, the lack of an independent method for measuring the pressure (such as pressure wires) is a limitation.

For non-Cartesian sequences, off-resonance effects are common due to the often long readout durations, in which effects such as eddy-currents contribute to trajectory deviation throughput the readout. We aimed to reduce these effects by keeping the spiral readout durations short (2.5 ms), which however prolonged the acquisition times for the spiral sequences. A common source of off-resonance in spiral imaging is the signal from fat, which is present in in-vivo imaging. In the phantom experiments performed, fat-suppression was excluded. The need for fat-suppression in clinical imaging will prolong TE, i.e. the possibility for low TE will be reduced in the spiral sequences [55]. Simulations performed on our MR system indicates that both 3D throughplane PC and 4D PC sequences used in this work can be used with a spectral-spatial excitation pulse [30] and still achieve TE below 2 ms. We also observed a less smooth background phase offset variation in the spiral datasets as compared to the Cartesian sequences, with minor streak artifacts present. This type of background phase offset variations are likely more difficult to correct for using polynomial fitting procedures.

Conclusion

In conclusion, our results show that the use of short-TE volumetric phase contrast allows accurate quantification of the maximum velocity in the investigated restriction model, as well as determination of its spatial position, as compared to CFD simulations. For shortest TE, spiral readouts presented better agreement with such simulations for average and peak velocities than Cartesian readouts, while our results show less good agreement concerning flow in the stenotic region. Spiral encoding also produced streamline visualizations with least noise and best resemblance to a CFD simulations.

Figure captions

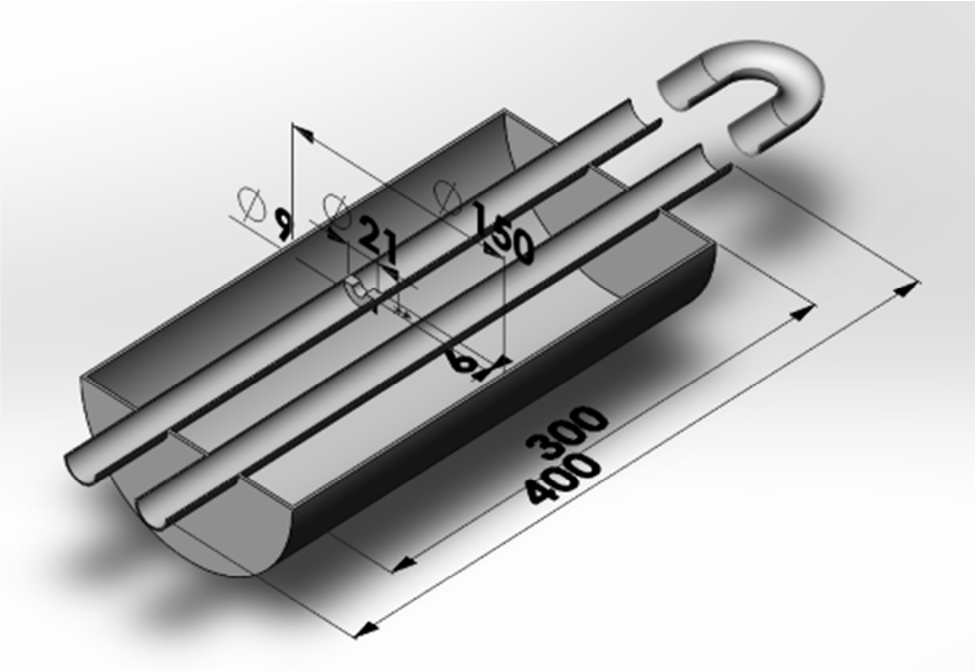

Fig 1. A cutaway illustration including dimensions (in units of mm) of the phantom used. The inlet (left) tube contained a sharp-edged restriction with a central orifice. On the back side of the phantom, outside the scanner, the two tubes were connected, thus forming a closed and steady flow system via the water pump. Both tubes were contained in a water-filled cylinder, providing stability and static regions used for phase correction.

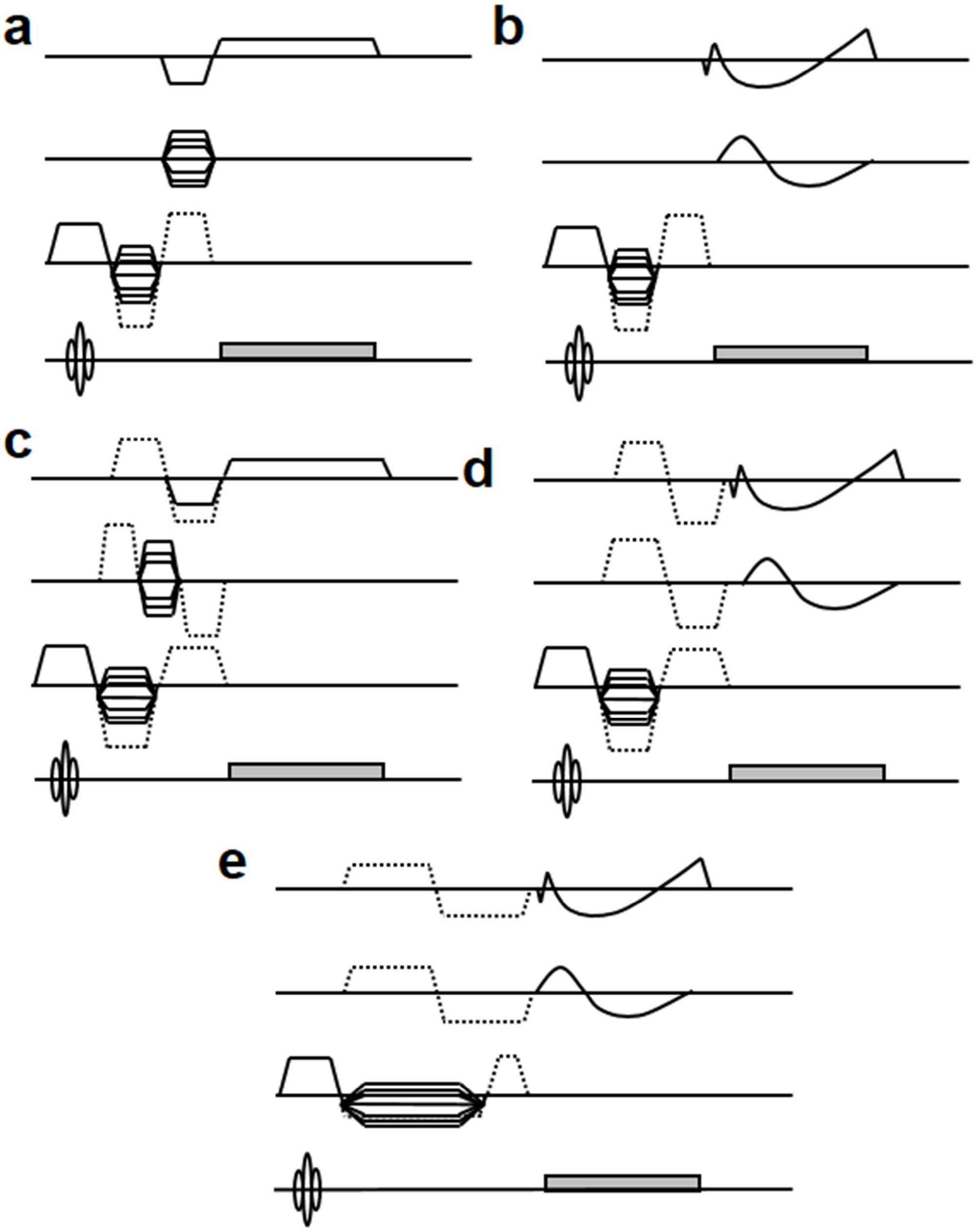

Fig 2. Conceptual overview of the pulse sequences used. a) 3D throughplane PC with Cartesian readout scheme. b) 3D throughplane PC with spiral readout. c) 4D PC with Cartesian readout. d) 4D PC with spiral readout. e) 4D PC with spiral readout and prolonged TE. Velocity-encoding is performed by the bipolar gradient pair immediately after slice selection and the RF pulse (dotted lines). Data acquisition is performed during the readout marked by grey boxes at the lower lines. For both 3D throughplane PC and 4D PC sequence types, spoiler gradients applied in all directions terminated the sequences (not shown).

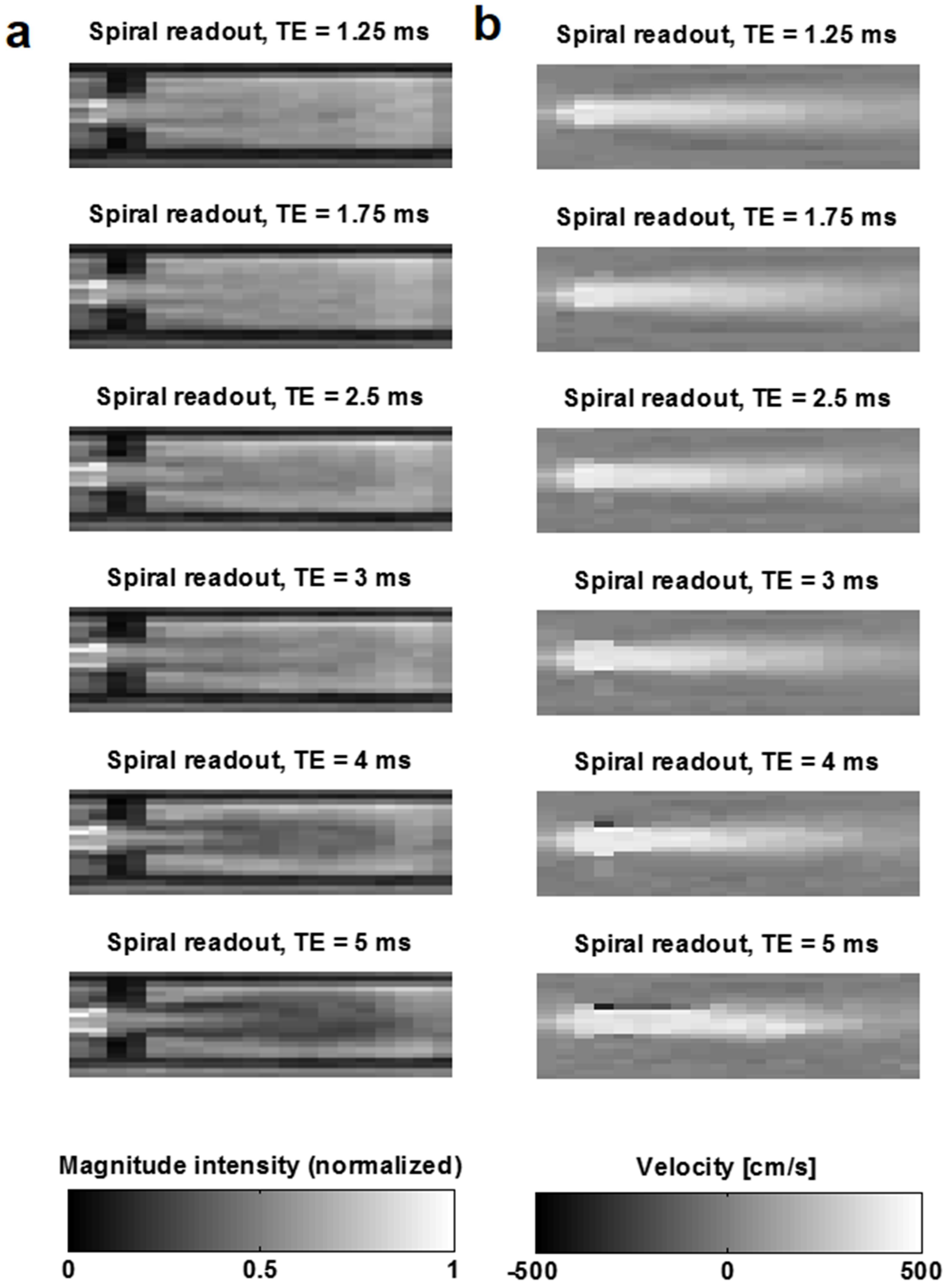

Fig 3. Images of the flow jet, acquired with untriggered 3D throughplane PC sequences. The left column (a) shows the magnitude intensity values, and the right column (b) displays the corresponding velocity images, with velocity encoding along the jet. The intensity values have been normalized to the highest intensity found in any acquired 3D throughplane PC dataset.

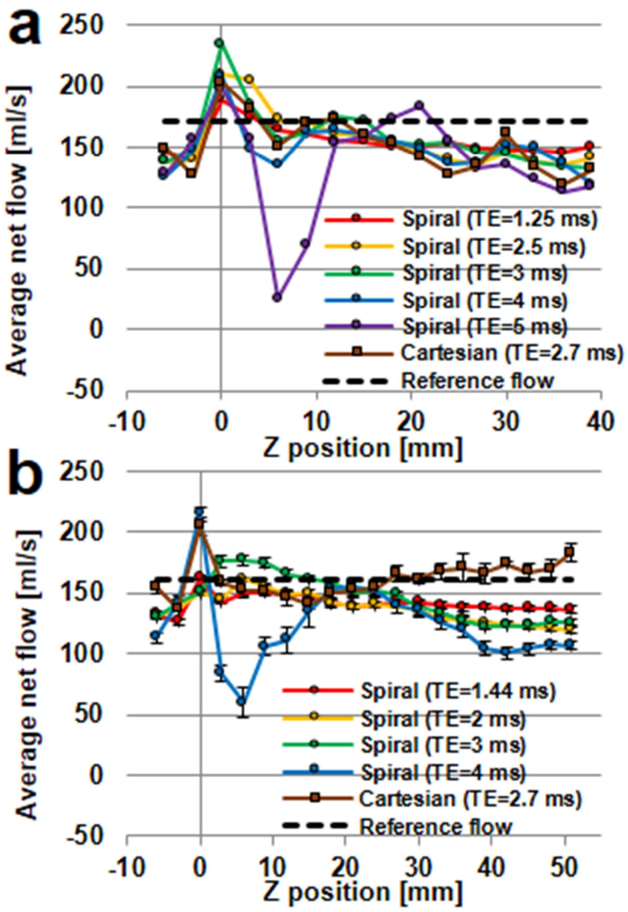

Fig 4. Average net flow in the direction of the jet, measured by untriggered 3D throughplane PC sequences (a) and triggered 4D PC sequences (b), for different echo times. Dotted line represents the reference flow, measured with a conventional 2D throughplane PC sequence 5 cm upstream of the restriction (Z=- 50 mm, not shown in figure).The restriction is positioned at Z= 0 cm.

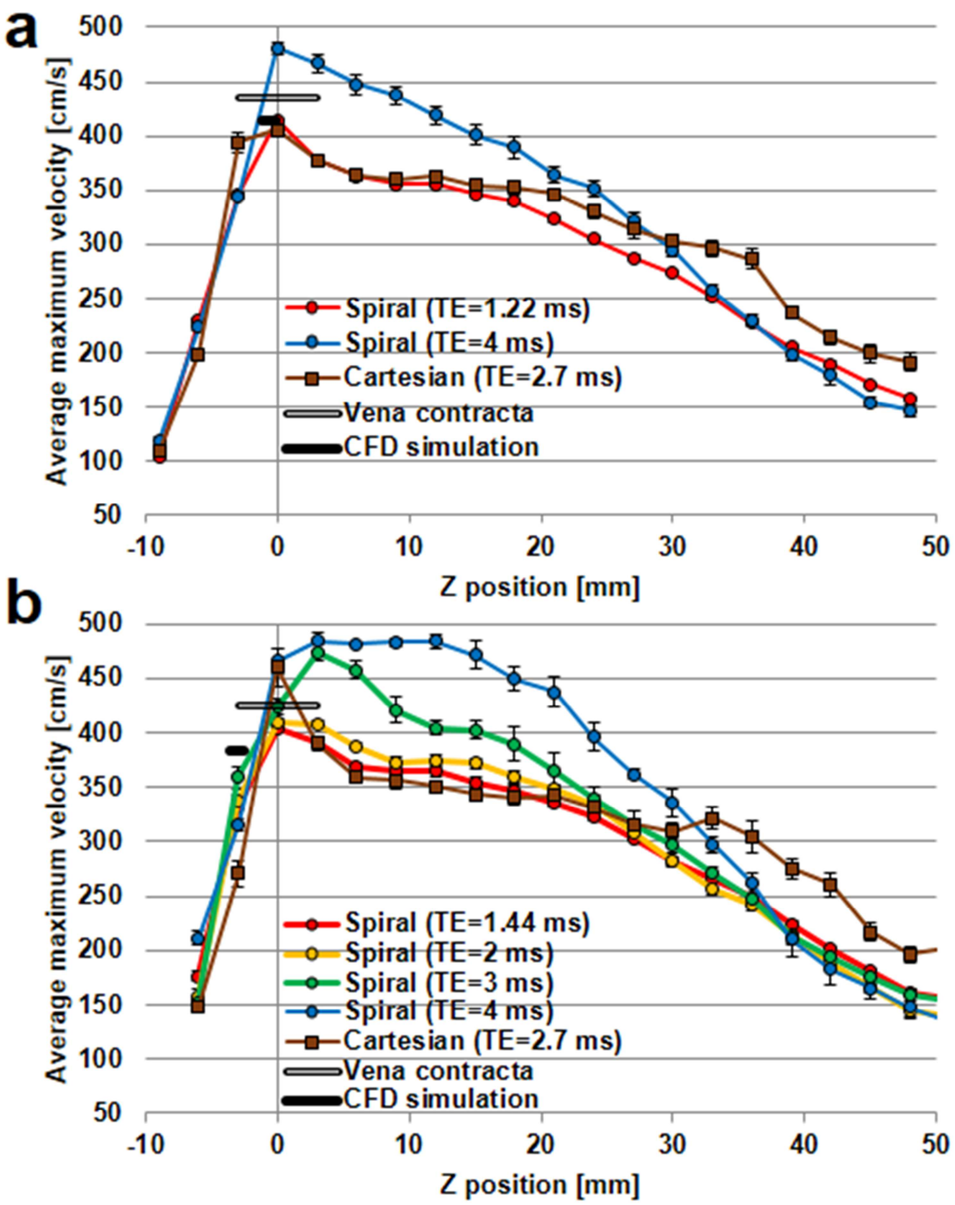

Fig 5. Average maximum velocities measured with 3D throughplane PC (a) and 4D PC (b). The black line represents the maximum velocity and its position derived from CFD simulations, and the hollow line the theoretically derived velocity in vena contracta. The position of the theoretically derived vena contracta velocity is assumed to be inside the orifice. The error bars represent ±standard error of the mean.

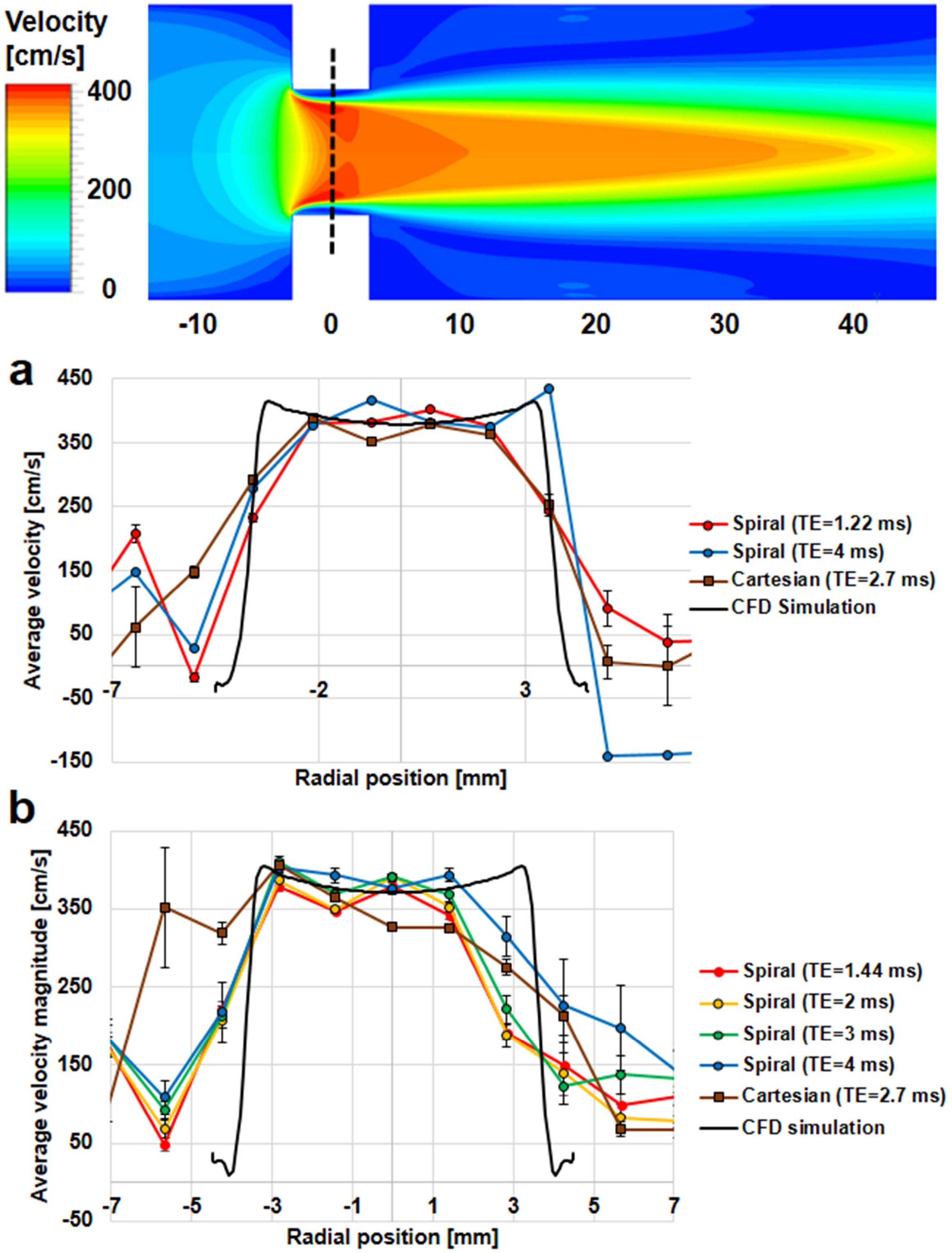

Fig 6. Top: the velocity distribution across the restriction (velocity magnitude) from CFD simulations. Below: Cross-sectional line profiles in the centre of the restriction (location marked with dotted line in top figure) for the 3D throughplane PC sequences (a) and the 4D PC sequences (b). The maximum velocity magnitude from the CFD simulation ($v_{CFD,max}$) is found inside the restriction, but does not lay on the central axis. Instead, $v_{CFD,max}$ is positioned close to the walls of the plate. Error bars represent ±standard error of the mean.

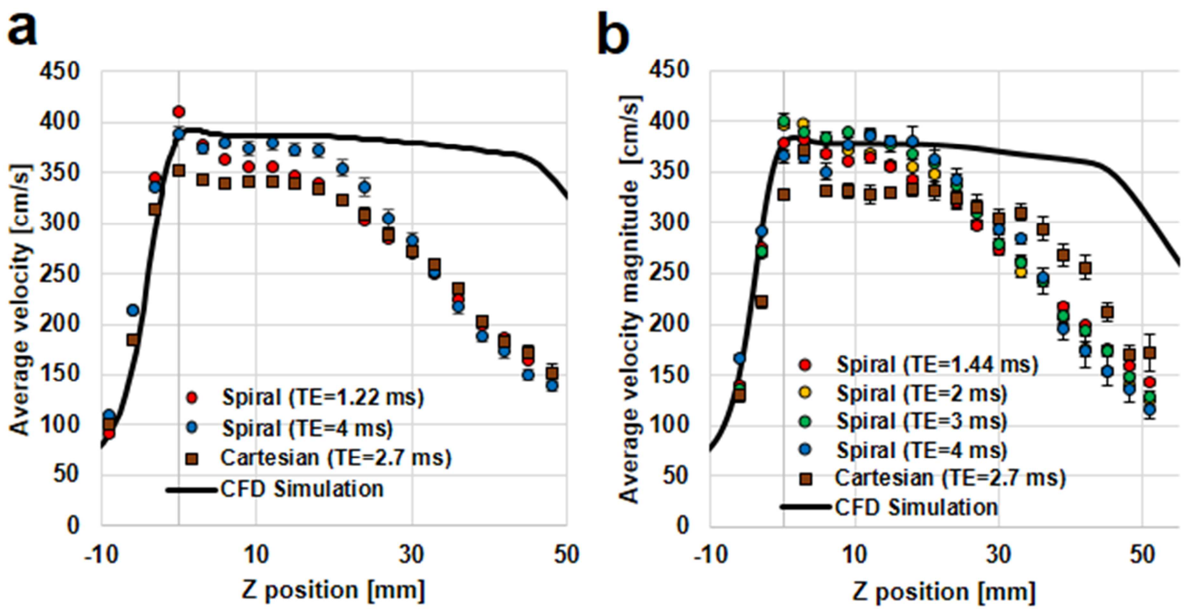

Fig 7 Average velocities along the central axis of the restriction, measured with 3D throughplane PC (a) and 4D PC (b) (velocity magnitude) Black solid line represents CFD-derived velocities in the direction of the jet. Error bars represent standard deviation of the mean.

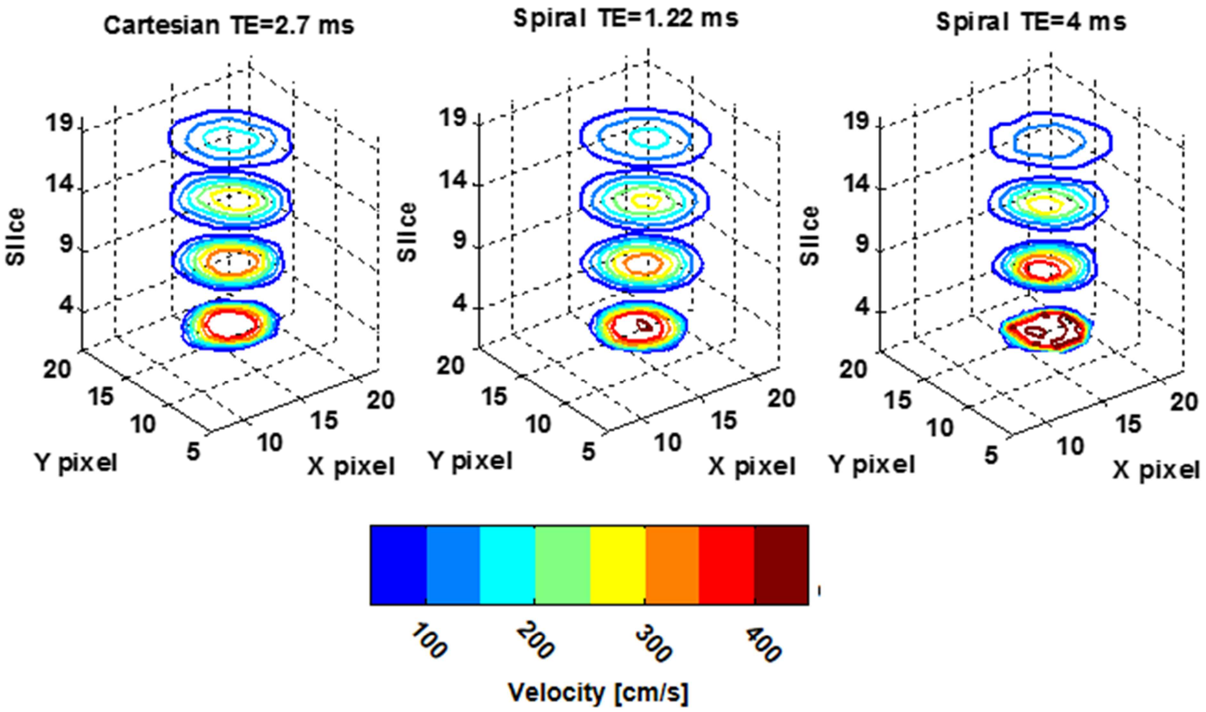

Fig 8 Contour illustrations of the jet shape, depicted by 3D throughplane PC sequences with Cartesian readout, TE=2.7 ms (a), and spiral readouts with TE=1.22 ms (b) and TE=4 (c) ms. The lowest contour plane is located in the centre of the restriction, while the upper contour plane is located most distal to the restriction.

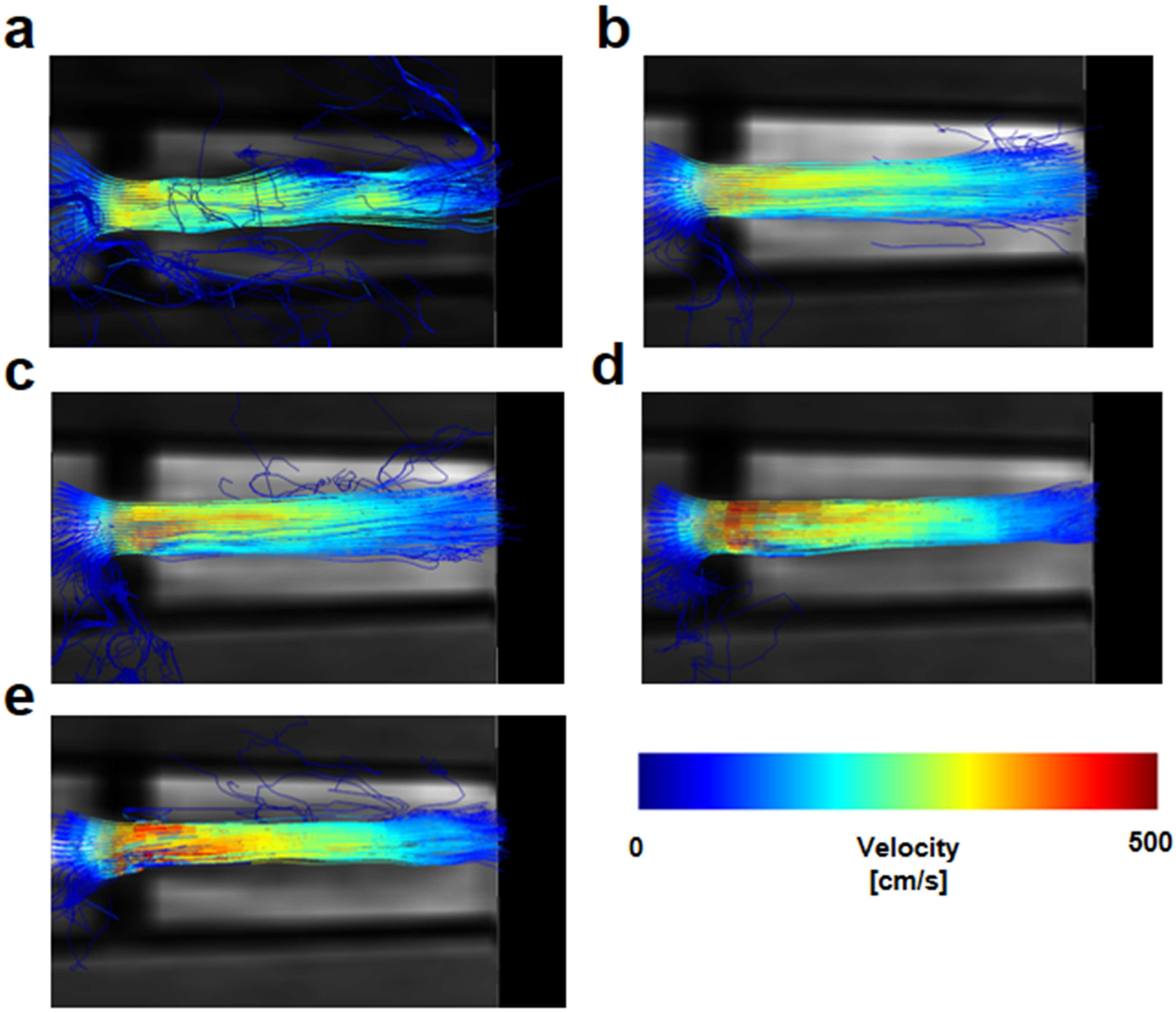

Fig 9 Streamline visualizations of the jet, created from the 4D PC sequences. 4D PC with Cartesian readout and TE=2.7 ms (a), 4D PC with spiral readout and TE=1.44 ms, (b)TE=2 ms (c), 3 ms (d) and 4 ms (e), respectively.

Table 1a. Overview of the sequence-specific parameters used

Parameter	3D throughplane PC		4D-PC		Ref. scan (2D throughplane PC)
	Cartesian	spiral	Cartesian	spiral	
TE [ms]°	2.7	1.22, 4	2.7	1.4, 4	n.a
TE [ms]*	2.7	1.25, 2.5, 3, 4, 5	n.a	n.a	11.7
TR [ms]°	5.3	5.6, 8.4	5.4	6.4, 9	n.a
TR [ms]*	5.3, 6,8,10	5.6,6.9,7.4,8.4,9.4	n.a	n.a	18.7
VENC [cm s^{-1}]	500	500	500	500	70-200
Scan time [m:s]	23:22°†	08:49°†	18:00°†	08:42°†	01:22*
Flip angle	10	10	10	10	10
Voxel size [RL,AP,FH]	1.4×1.4×3	1.4×1.4×3	1.4×1.4×3	1.4×1.4×3	0.7×0.7×6
FOV [RL, AP,FH]	320×320×60	320×320×60	320×320×60	320×320×60	320×258×6
NSA	1	1	1	1	6-8
Turbo-factor	4	4	4	4	1
Acquired timeframes °	13°	9-13°	7°	5-7°	1

† Estimated scan time when simulated at a heart rate of 59 beats per minute

° Triggered

* Untriggered

Table 1b. Acceleration sensitivities for the triggered 4D sequences used, expressed as the acceleration inducing a phase angle of π.

Acceleration sensitivity [m s^{-2}]	X direction	Y direction	Z direction
Cartesian (TE=2.7 ms)	7143	8333	6250
Spiral (TE=1.44 ms)	7142	6250	6250
Spiral (TE=2 ms)	5000	5000	4545
Spiral (TE=3 ms)	3333	3125	2631
Spiral (TE=4 ms)	2500	2500	2500

Table 2a. Mean flow, maximum velocity and peak pressure gradient in the centre of the restriction as measured with triggered sequences. For flow, the percentage difference presented is with respect to the reference flow measured at each scan occasion, while the maximum velocity difference is with respect to the CFD-derived maximum velocity. The peak pressure difference gradient is calculated using Eq. 1 and compared with the value obtained from CFD simulations. Note that the velocities and flow rates differs between the columns due to the variation in flow rate between measurement sessions. Presented values are averaged over all acquired timeframes and presented with ±standard error of the mean.

		3D throughplane PC		4D PC	
		Cartesian	spiral	Cartesian	spiral
TE=shortest (see Table 1)	Flow rate [ml/s]	164±2	186±1	205±7	163±2
	Difference [%][1]	-0.6	12	27	0.8
	Maximum velocity [cm/s]	405±4	414±2	460±17	404±3
	Difference [%][2]	-2.3	-0.1	13	-0.5
	Peak pressure gradient [mmHg]	62±1	64±1	80±6	61±1
	Difference [%][2]	8.8	14	48	13

[1] Difference to the reference flow measured by 2D throughplane PC

[2] Difference to the values obtained from CFD simulations

Table 2b. Mean flow, maximum velocity and peak pressure gradient in the centre of the restriction as measured with triggered 4D spiral sequences. For flow, the percentage difference presented is with respect to the reference flow measured at each scan occasion, while the maximum velocity difference is with respect to the CFD-derived maximum velocity. The peak pressure difference gradient is calculated using Eq. 1 and compared with the value obtained from CFD simulations. Presented values are averaged over all acquired timeframes and presented with ±standard error of the mean.

	4D PC spiral		
	TE=2 ms	TE= 3 ms	TE= 4ms
Flow [ml/s]	151±1	151±2	215±6
Difference [%]	-6.7	-6.4	33
Maximum velocity [cm/s]	409±4	423±7	466±11
Difference [%]	0.9	4.3	15
Peak pressure gradient [mmHg]	63±1	67±2	82±4
Difference [%]	16	24	50

Funding

EH was funded by Swedish Research Council (VR 621-2008-2949 and VR K2009-65X-14599-07-3), and Region of Scania, Sweden.

KMB is an employee of Philips Healthcare. Funding from the Swedish Foundation for Strategic Research, SM09-0070, is gratefully acknowledged.

References

1. Sondergaard L, Stahlberg F, Thomsen C (1999) Magnetic resonance imaging of valvular heart disease. J Magn Reson Imaging 10 (5):627-638
2. Lima CO, Sahn DJ, Valdes-Cruz LM, Goldberg SJ, Barron JV, Allen HD, Grenadier E (1983) Noninvasive prediction of transvalvular pressure gradient in patients with pulmonary stenosis by quantitative two-dimensional echocardiographic Doppler studies. Circulation 67 (4):866-871
3. Hatle L, Brubakk A, Tromsdal A, Angelsen B (1978) Noninvasive assessment of pressure drop in mitral stenosis by Doppler ultrasound. Br Heart J 40 (2):131-140
4. Quinones MA, Otto CM, Stoddard M, Waggoner A, Zoghbi WA, Doppler Quantification Task Force of the N, Standards Committee of the American Society of E (2002) Recommendations for quantification of Doppler echocardiography: a report from the Doppler Quantification Task Force of the Nomenclature and Standards Committee of the American Society of Echocardiography. J Am Soc Echocardiogr 15 (2):167-184
5. Otto CM (2006) Valvular aortic stenosis: disease severity and timing of intervention. J Am Coll Cardiol 47 (11):2141-2151
6. Rich JD, Shah SJ, Swamy RS, Kamp A, Rich S (2011) Inaccuracy of Doppler echocardiographic estimates of pulmonary artery pressures in patients with pulmonary hypertension: implications for clinical practice. Chest 139 (5):988-993
7. Cawley PJ, Maki JH, Otto CM (2009) Cardiovascular magnetic resonance imaging for valvular heart disease: technique and validation. Circulation 119 (3):468-478
8. Mohiaddin RH, Kilner PJ, Rees S, Longmore DB (1993) Magnetic resonance volume flow and jet velocity mapping in aortic coarctation. J Am Coll Cardiol 22 (5):1515-1521
9. Sondergaard L, Stahlberg F, Thomsen C, Stensgaard A, Lindvig K, Henriksen O (1993) Accuracy and precision of MR velocity mapping in measurement of stenotic cross-sectional area, flow rate, and pressure gradient. J Magn Reson Imaging 3 (2):433-437
10. Holmqvist C, Oskarsson G, Stahlberg F, Thilen U, Bjorkhem G, Laurin S (1999) Functional evaluation of extracardiac ventriculopulmonary conduits and of the right ventricle with magnetic resonance imaging and velocity mapping. Am J Cardiol 83 (6):926-932
11. Defrance C, Bollache E, Kachenoura N, Perdrix L, Hrynchyshyn N, Bruguiere E, Redheuil A, Diebold B, Mousseaux E (2012) Evaluation of aortic valve stenosis using cardiovascular magnetic resonance: comparison of an original semiautomated analysis of phase-contrast cardiovascular magnetic resonance with Doppler echocardiography. Circ Cardiovasc Imaging 5 (5):604-612
12. O'Brien KR, Gabriel RS, Greiser A, Cowan BR, Young AA, Kerr AJ (2009) Aortic valve stenotic area calculation from phase contrast cardiovascular magnetic resonance: the importance of short echo time. J Cardiovasc Magn Reson 11:49
13. O'Brien KR, Cowan BR, Jain M, Stewart RA, Kerr AJ, Young AA (2008) MRI phase contrast velocity and flow errors in turbulent stenotic jets. J Magn Reson Imaging 28 (1):210-218

14. O'Brien KR, Myerson SG, Cowan BR, Young AA, Robson MD (2009) Phase contrast ultrashort TE: A more reliable technique for measurement of high-velocity turbulent stenotic jets. Magn Reson Med 62 (3):626-636

15. Nayak KS, Hu BS, Nishimura DG (2003) Rapid quantitation of high-speed flow jets. Magn Reson Med 50 (2):366-372

16. Steinman DA, Ethier CR, Rutt BK (1997) Combined analysis of spatial and velocity displacement artifacts in phase contrast measurements of complex flows. J Magn Reson Imaging 7 (2):339-346

17. Nilsson A, Bloch KM, Toger J, Heiberg E, Stahlberg F (2013) Accuracy of four-dimensional phase-contrast velocity mapping for blood flow visualizations: a phantom study. Acta Radiol 54 (6):663-671

18. Giese D, Haeberlin M, Barmet C, Pruessmann KP, Schaeffter T, Kozerke S (2012) Analysis and correction of background velocity offsets in phase-contrast flow measurements using magnetic field monitoring. Magn Reson Med 67 (5):1294-1302

19. Lankhaar JW, Hofman MB, Marcus JT, Zwanenburg JJ, Faes TJ, Vonk-Noordegraaf A (2005) Correction of phase offset errors in main pulmonary artery flow quantification. J Magn Reson Imaging 22 (1):73-79

20. Thunberg P, Emilsson K, Rask P, Kahari A (2012) Flow and peak velocity measurements in patients with aortic valve stenosis using phase contrast MR accelerated with k-t BLAST. Eur J Radiol 81 (9):2203-2207

21. Wigstrom L, Sjoqvist L, Wranne B (1996) Temporally resolved 3D phase-contrast imaging. Magn Reson Med 36 (5):800-803

22. Markl M, Chan FP, Alley MT, Wedding KL, Draney MT, Elkins CJ, Parker DW, Wicker R, Taylor CA, Herfkens RJ, Pelc NJ (2003) Time-resolved three-dimensional phase-contrast MRI. J Magn Reson Imaging 17 (4):499-506

23. Bogren HG, Buonocore MH (1999) 4D magnetic resonance velocity mapping of blood flow patterns in the aorta in young vs. elderly normal subjects. J Magn Reson Imaging 10 (5):861-869

24. Stalder AF, Russe MF, Frydrychowicz A, Bock J, Hennig J, Markl M (2008) Quantitative 2D and 3D phase contrast MRI: optimized analysis of blood flow and vessel wall parameters. Magn Reson Med 60 (5):1218-1231

25. Dyverfeldt P, Kvitting JP, Sigfridsson A, Engvall J, Bolger AF, Ebbers T (2008) Assessment of fluctuating velocities in disturbed cardiovascular blood flow: in vivo feasibility of generalized phase-contrast MRI. J Magn Reson Imaging 28 (3):655-663

26. Hope MD, Meadows AK, Hope TA, Ordovas KG, Saloner D, Reddy GP, Alley MT, Higgins CB (2010) Clinical Evaluation of Aortic Coarctation With 4D Flow MR Imaging. Journal of Magnetic Resonance Imaging 31 (3):711-718

27. Hope MD, Meadows AK, Hope TA, Ordovas KG, Reddy GP, Alley MT, Higgins CB (2008) Evaluation of bicuspid aortic valve and aortic coarctation with 4D flow magnetic resonance imaging. Circulation 117 (21):2818-2819

28. Gu T, Korosec FR, Block WF, Fain SB, Turk Q, Lum D, Zhou Y, Grist TM, Haughton V, Mistretta CA (2005) PC VIPR: a high-speed 3D phase-contrast method for flow quantification and high-resolution angiography. AJNR Am J Neuroradiol 26 (4):743-749

29. Johnson KM, Lum DP, Turski PA, Block WF, Mistretta CA, Wieben O (2008) Improved 3D phase contrast MRI with off-resonance corrected dual echo VIPR. Magn Reson Med 60 (6):1329-1336

30. Sigfridsson A, Petersson S, Carlhall CJ, Ebbers T (2012) Four-dimensional flow MRI using spiral acquisition. Magn Reson Med 68 (4):1065-1073

31. Janiczek RL, Blackman BR, Roy RJ, Meyer CH, Acton ST, Epstein FH (2011) Three-dimensional phase contrast angiography of the mouse aortic arch using spiral MRI. Magn Reson Med 66 (5):1382-1390

32. Nordmeyer S, Riesenkampff E, Messroghli D, Kropf S, Nordmeyer J, Berger F, Kuehne T (2013) Four-dimensional velocity-encoded magnetic resonance imaging improves blood flow quantification in patients with complex accelerated flow. J Magn Reson Imaging 37 (1):208-216

33. Bock J, Frydrychowicz A, Lorenz R, Hirtler D, Barker AJ, Johnson KM, Arnold R, Burkhardt H, Hennig J, Markl M (2011) In vivo noninvasive 4D pressure difference mapping in the human aorta: phantom comparison and application in healthy volunteers and patients. Magn Reson Med 66 (4):1079-1088

34. Bley TA, Johnson KM, Francois CJ, Reeder SB, Schiebler ML, B RL, Consigny D, Grist TM, Wieben O (2011) Noninvasive assessment of transstenotic pressure gradients in porcine renal artery stenoses by using vastly undersampled phase-contrast MR angiography. Radiology 261 (1):266-273

35. Nett E RL, García-Rodríguez S, Roldan A, Wieben O, Johnson K Pressure Difference Measurements in Stenotic Flow Phantom: Comparison of 4D flow MRI, Computational Fluid Dynamics, and Pressure Wire Measurements. In: Proc. Intl. Soc. Mag. Reson. Med., Salt Lake City, USA, 2013.

36. Marshall I (2010) Computational simulations and experimental studies of 3D phase-contrast imaging of fluid flow in carotid bifurcation geometries. J Magn Reson Imaging 31 (4):928-934

37. Bernstein MA, Shimakawa A, Pelc NJ (1992) Minimizing TE in moment-nulled or flow-encoded two- and three-dimensional gradient-echo imaging. J Magn Reson Imaging 2 (5):583-588

38. Carlsson M, Toger J, Kanski M, Bloch KM, Stahlberg F, Heiberg E, Arheden H (2011) Quantification and visualization of cardiovascular 4D velocity mapping accelerated with parallel imaging or k-t BLAST: head to head comparison and validation at 1.5 T and 3 T. Journal of Cardiovascular Magnetic Resonance 13

39. Massey BS (1989) Mechanics of fluids. 6. ed edn. Chapman & Hall, London

40. Chisholm D (1983) Two-phase flow in pipelines and heat exchangers. G. Godwin in association with Institution of Chemical Engineers, London ; New York

41. Roul MK, Dash SK (2012) Single-Phase and Two-Phase Flow Through Thin and Thick Orifices in Horizontal Pipes. J Fluids Eng 134 (9)

42. Patankar SV, Spalding DB (1972) A calculation procedure for heat, mass and momentum transfer in three-dimensional parabolic flows. Int J Heat Mass Transf 15 (10):1787-1806

43. Yakhot V, Orszag SA, Thangam S, Gatski TB, Speziale CG (1992) Development of Turbulence Models for Shear Flows by a Double Expansion Technique. Physics of Fluids a-Fluid Dynamics 4 (7):1510-1520

44. Menter FR (1994) 2-Equation Eddy-Viscosity Turbulence Models for Engineering Applications. Aiaa Journal 32 (8):1598-1605

45. Speziale CG, Sarkar S, Gatski TB (1991) Modeling the Pressure Strain Correlation of Turbulence - an Invariant Dynamic-Systems Approach. Journal of Fluid Mechanics 227:245-272

46. Boussinesq J (1877) Essai sur la théorie des eaux courantes. Mémoires présentés par divers savants à l'Académie des sciences de l'Institut national de France, vol [2 sér] t XXIII, no 1; t XXIV, no 2. Imprimerie nationale, Paris

47. Schmitt FG (2007) About Boussinesq's turbulent viscosity hypothesis: historical remarks and a direct evaluation of its validity. Comptes Rendus Mecanique 335 (9-10):617-627

48. Tayler AB, Holland DJ, Sederman AJ, Gladden LF (2011) Time resolved velocity measurements of unsteady systems using spiral imaging. J Magn Reson 211 (1):1-10

49. Stahlberg F, Thomsen C, Sondergaard L, Henriksen O (1994) Pulse sequence design for MR velocity mapping of complex flow: notes on the necessity of low echo times. Magn Reson Imaging 12 (8):1255-1262

50. Oshinski JN, Ku DN, Bohning DE, Pettigrew RI (1992) Effects of acceleration on the accuracy of MR phase velocity measurements. J Magn Reson Imaging 2 (6):665-670

51. Kouwenhoven M, Hofman MB, Sprenger M (1995) Motion induced phase shifts in MR: acceleration effects in quantitative flow measurements--a reconsideration. Magn Reson Med 33 (6):766-777

52. Kilner PJ, Manzara CC, Mohiaddin RH, Pennell DJ, Sutton MG, Firmin DN, Underwood SR, Longmore DB (1993) Magnetic resonance jet velocity mapping in mitral and aortic valve stenosis. Circulation 87 (4):1239-1248

53. Popp RL, Teplitsky I (1989) Lessons from in vitro models of small, irregular, multiple and tunnel-like stenoses relevant to clinical stenoses of valves and small vessels. J Am Coll Cardiol 13 (3):716-722

54. Frayne R, Rutt BK (1995) Understanding acceleration-induced displacement artifacts in phase-contrast MR velocity measurements. J Magn Reson Imaging 5 (2):207-215

55. Nayak KS, Pauly JM, Kerr AB, Hu BS, Nishimura DG (2000) Real-time color flow MRI. Magn Reson Med 43 (2):251-258